ELSEVIER

Journal of Alloys and Compounds 434–435 (2007) 229–233

Journal of ALLOYS AND COMPOUNDS

www.elsevier.com/locate/jallcom

Surface properties and activity of Fe–Ni–B ternary glasses

P. Patsalas [a,*], A. Lekatou [a], E. Pavlidou [b], S. Foulias [c], M. Kamaratos [c], G.A. Evangelakis [c], A.R. Yavari [d]

[a] *University of Ioannina, Department of Materials Science and Engineering, GR-45110 Ioannina, Greece*
[b] *Aristotle University of Thessaloniki, Department of Physics, GR-54124 Thessaloniki, Greece*
[c] *University of Ioannina, Department of Physics, GR-45110 Ioannina, Greece*
[d] *LTPCM-CNRS, Institut National Polytechnique de Grenoble, 1130 rue de la Piscine, BP 75, 38402 St Martin d'Hères Campus, France*

Available online 15 December 2006

Abstract

The surface structure, composition and corrosion behavior of metallic glass (MG) ribbons of the Fe–Ni–B system, with nominal composition $Fe_{40}Ni_{40}B_{20}$ are investigated by X-ray diffraction, Auger electron spectroscopy (AES) and energy dispersive X-ray spectroscopy (EDS). We found that the surface is Fe enriched at the expense of both Ni and B, while exposure to 200 eV N^+ and Ar^+ plasma modifies slightly the top surface layer further enriching the surface with Fe; in the case of N^+, strong incorporation of N is detected indicating the formation of nitride phases. The corrosion behavior of the Fe–Ni–B surfaces was studied by electrochemical techniques in aquatic solutions of NaCl, NaOH, HNO_3 and HCl. Corrosion properties are very satisfactory compared to other MGs and engineering crystalline alloys with similar base compositions.

Keywords: Metallic glasses; Surfaces and interfaces; Gas–solid interactions; Composition fluctuations; Corrosion

1. Introduction

Metallic glasses are a special category of materials that are characterized by their amorphous structure and metallic bonds. Owing to their disordered structure, metallic glasses possess several unique properties that make them attractive for mechanical and tribological applications [1,2]. The superior mechanical performance is mainly attributed to the absence of dislocations that prevents plastic deformation. The correlation between the functional properties of MGs and their microstructure has been established based on their bulk microstructure. Many methods were used to modify and tailor the microstructure and functional properties of MGs, among them is ion irradiation [3,4].

Although in industrial conditions the surface is usually exposed to the working environment, the surface structure and properties of MGs have received less attention, so far. A very important surface property is the corrosion resistance of MGs, which has received recently particular attention [5–8]. The superior corrosion resistance of MGs is also attributed to the absence of crystalline defects such as grain boundaries and second phase precipitates. Their homogeneity may ensure the formation of a uniform passive film and drastically reduce the risk of localized corrosion. The corrosion behavior of metallic glasses is mainly determined by the nature of the alloying elements [9,10].

In this work, we study the surface properties and the surface modifications after ion irradiation of MGs of the Fe–Ni–B system, which are promising materials fulfilling the requirements for various industrial applications [2]. The surface and bulk structure and composition of ribbons of the Fe–Ni–B system, with nominal composition $Fe_{40}Ni_{40}B_{20}$ are investigated by X-ray diffraction (XRD), Auger electron spectroscopy (AES) and energy dispersive X-ray spectroscopy (EDS). In order to investigate their structural and compositional stability, the Fe–Ni–B surfaces have been also exposed to 200 eV N^+ and Ar^+ rf-plasma discharge, which is similar to many industrial processes. Finally, the corrosion behavior of the Fe–Ni–B surfaces is studied by electrochemical techniques in aquatic solutions of 3.5% NaCl, 1 M NaOH, 1 M HNO_3, 1 M HCl, concentrated HNO_3 and deionized H_2O.

2. Experimental

The Fe–Ni–B ribbons were grown by the melt-spinning technique [4]. Surface processing using Ar^+ or N^+ plasma were performed in a high-vacuum ($P_b = 5 \times 10^{-7}$ mbar) chamber using a 15 sccm gas flow. The specimens were mounted on the anode electrode, which was connected to a rf power supply with a matching network that provided a bias voltage of 200 V.

* Corresponding author. Tel.: +30 26510 97146; fax: +30 26510 98673.
E-mail address: ppats@cc.uoi.gr (P. Patsalas).

0925-8388/$ – see front matter © 2006 Published by Elsevier B.V.
doi:10.1016/j.jallcom.2006.08.104

The X-ray diffraction (XRD) experiments have been carried out in a Siemens D-5000 2-circle diffractometer in Bragg–Brentano ($\theta - 2\theta$ scan) and grazing incidence ($\alpha - 2\theta$ scan, $\alpha = 2^\circ$) geometries. The apparatus is equipped with parallel beam optics consisting of a Goebel mirror to focus the divergent X-ray beam and a Soller slit array in front of the detector. The high voltage on the Cu-anode was 40 kV and the electron current was 40 mA. The Goebel mirror separated spatially the Cu K_β and Cu K_α lines; the Cu K_β line has been cut by a 1 mm slit. The scan step was $2\theta = 0.04^\circ$ and the scan speed varied between 0.5 and 0.05 °/min.

The [Fe]/[Ni] ratio in the bulk (penetration depth ~4 μm) of the specimens has been determined by electron dispersive X-ray spectroscopy (EDS) using the X-ray analyzer of JEOL conventional scanning electron microscope (SEM). The Auger electron spectroscopy (AES) spectra were recorded in an ultra-high vacuum system (base pressure $< 1 \times 10^{-9}$ mbar) equipped with a physical electronics electron gun and a cylindrical mirror electron analyzer operating at 650 V. The energy and current of the excitation electron beam were 2.5 keV and 1.8 mA, respectively. The AES spectra were recorded using a lock-in amplifier in differential mode (dN/dE). Each experimental run started measuring two reference samples of pure Ta and sp^2-bonded a-C in order to evaluate the profile and the energy position of the Ta and C_{KLL} AES peaks for validation purposes.

Anodic potentiodynamic polarization tests in rectangular ribbon polished specimens of 150 mm^2 surface area were carried out according to the ASTM G5-94 standard [11], in the aqueous aerated solutions: 1M HNO_3, concentrated (c.) HNO_3, 1M NaOH, 3.5 wt.% NaCl and 1M HCl, as well as in deionized water (the latter) for comparison. A three-electrode cell was used consisting of a working electrode, a saturated (s.) AgCl electrode as the reference electrode and a Pt electrode as the counter electrode. The experiments were conducted at room temperature. The potential was controlled and the current density was measured by a potentiostat/galvanostat (model GILL AC by ACM Instruments). The scan rate employed was 10 mV/min. All the potential values presented in this work are expressed on the s. AgCl scale ($E_{AgCl} = E_{SHE} + 0.20$ mV). Corrosion current densities were determined by the Tafel slope technique. Corrosion rates were calculated based on the Faraday law. A cyclic potentiodynamic polarization test was also conducted, to determine the susceptibility of the amorphous alloy to localized corrosion, in a 3.5 wt.% NaCl aqueous solution, at room temperature, according to the ASTM G61-86 standard [12].

3. Results and discussion

The Fe–Ni–B ribbons have been investigated by SEM. No crystalline inclusions were detected in the micron scale. The ribbons are homogeneous and smooth. EDS spectra were acquired at various magnifications. The light elements such as B can be hardly identified in the set up used (only elements heavier than O can be safely identified). The ribbon did not exhibit any kind of impurities such as O; only some traces of C have been detected, but this is attributed to surface contamination. At all magnifications and at wide spatial distribution of measurements, EDS confirmed the nominal [Fe]/[Ni] = 1 ratio of the ribbons (Fe 40 at.%, Ni 40 at.%).

The sampling volume of EDS measurements is determined by the escape depth d_0 of the generated X-ray photons in the specimen. According to the law of Beer–Lambert as well as taking into account the composition of the ribbons ($Fe_{40}Ni_{40}B_{20}$) and the mass absorption coefficients of Fe, Ni, B and the density of the $Fe_{40}Ni_{40}B_{20}$ glass, d_0 is determined to be about 4 μm. Therefore, the EDS results can be safely considered as representative of the bulk properties of the specimens.

In order to determine the [B] concentration and the possible segregation phenomena on the surface of the ribbons we also studied them by AES, as shown in Fig. 1. AES clearly demonstrates the existence of B, which was not detected by

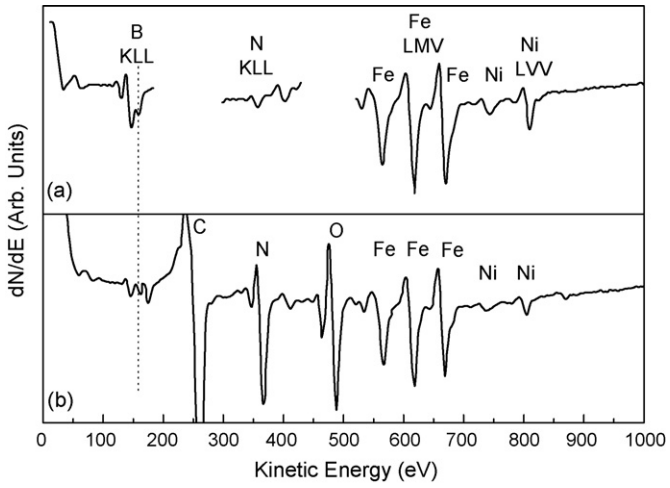

Fig. 1. AES spectra from (a) an as-received $Fe_{40}Ni_{40}B_{20}$ glass ribbon (the C_{KLL} and O_{KLL} peaks are not displayed for better clarity) and (b) the same ribbon after 15 min plasma nitridation (200 eV, N^+).

EDS. The C_{KLL} and O_{KLL} AES peaks, which are attributed to surface contamination, are not displayed for better clarity. For the quantitative determination of the surface composition we used the Ni(LVV), B(KLL) and Fe(LMV) peaks [13], as shown in Fig. 1a and taking into account the relative sensitivity of each peak at the particular used excitation energy [14]. The surface composition of the as-grown specimens is [Fe] = 75 at.%, [Ni] = 20 at.%, [B] = 5 at.%; i.e. $Fe_{75}Ni_{20}B_5$. We observe a surface segregation of Fe at the expense of Ni and B, driven possibly by the lower surface free energy of Fe compared to Ni and B [15]. After plasma nitridation (Fig. 1b), N is strongly incorporated on the glass surface. The [N] concentration is close to the sum [Fe] + [Ni] + [B]; in particular: [N]/([Fe] + [Ni] + [B]) = 0.6. Thus, the surface composition becomes $[Fe_{79}Ni_{11}B_{10}]N_{0.6}$. After nitridation the surface is further enriched in Fe accompanied by an increase in [B]. The former may be due to relaxation and diffusion of Fe atoms triggered by the collisions between Fe and N^+. Another explanation would be that the iron nitrides and boron nitrides are more stable than the nickel nitrides.

The structure of the Fe–Ni–B ribbons has been also studied by XRD in Bragg–Brentano and grazing incidence geometries. Fig. 2 shows representative XRD patterns in both geometries for a $Fe_{40}Ni_{40}B_{20}$ ribbon. In both cases, two wide, distinct peaks are manifested, which are characteristic of MGs. The one peak (at detection angle ~45°) corresponds to the first neighbor distance, while the other one, manifested at low angles, may correspond to second (or higher) neighbor distances. The grazing incidence experiments have been carried out with $\alpha = 2^\circ$ in order to minimize the analysis depth d; for $\alpha = 2^\circ$, $d \sim 130$ nm for the first neighbor peak, while for Bragg–Brentano experiments, $d \sim 1300$ nm for the first neighbor peak. The two peaks are observed at the same angular positions meaning that the ribbons are homogeneous in this scale (130–1300 nm) and the segregation phenomena observed in AES are very localized to the surface region (<5 nm).

The effect of plasma nitriding and Ar^+ bombardment (i.e. chemically active and inert plasma, respectively) on

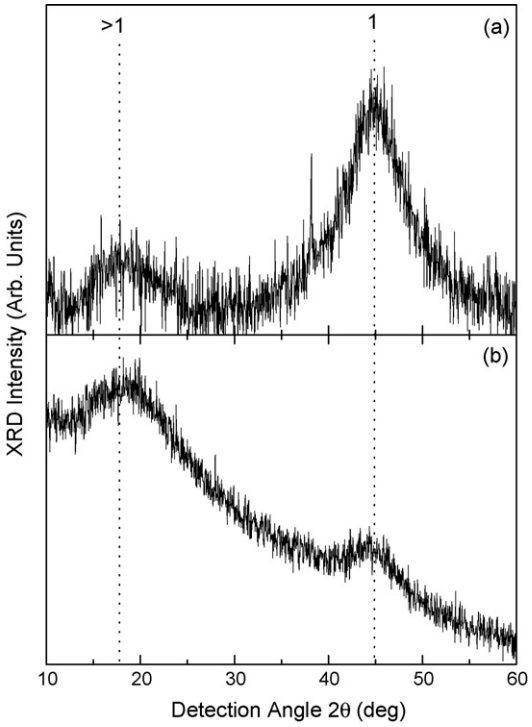

Fig. 2. XRD patterns from a representative $Fe_{40}Ni_{40}B_{20}$ glass ribbon in (a) Bragg–Brentano, and (b) grazing incidence ($\alpha = 2^\circ$) geometries. Two distinct, wide peaks are identified in both patterns; the one (at $2\theta \sim 45^\circ$) corresponds to the first neighbor-distance and the other to the second (or higher) neighbor distances.

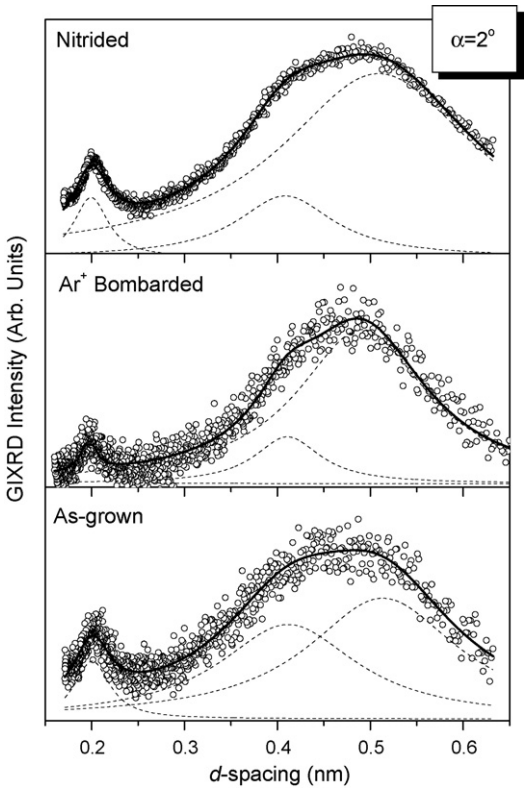

Fig. 3. XRD patterns in grazing incidence geometry for a pure $Fe_{40}Ni_{40}B_{20}$ ribbon (denoted 'as-grown') and after 200 eV Ar^+ and N^+ irradiation.

the microstructure of the ribbons has been studied by XRD exclusively in grazing incidence geometry, since the possible modifications are expected to occur in the top exposed layers as determined by SRIM calculations [16]. The corresponding XRD patterns after baseline subtraction are presented in Fig. 3. The *x*-axis is expressed in interatomic spacing *d* calculated from the detection angle using Bragg's law. We should note here that we will not attempt to quantitatively compare the contributions (area) of the first and higher-order neighbors, because they might be affected by the baseline. However, the *d*-spacing values alone can give valuable information about the microstructure of the ribbons.

The XRD patterns were deconvoluted to three Lorentzian peaks. The first one corresponds to the first neighbors and is rather sharp, showing that one kind of nearest neighbors exist. For higher-order neighbors there is very wide spread, characteristic of the glassy state. The first neighbor distance has been found to vary with the processing conditions. The values of the first neighbor distance for the various specimens are summarized in Fig. 4. The first neighbor distance of the as grown (unprocessed) ribbon was found to be about 0.201 nm, which is in fair agreement with the corresponding value reported by Sietsma and Thijesse [17] for the metal–boron (both Fe–B and Ni–B) distance. Therefore, we conclude that the nearest neighbors in our ribbons are the metal–B pairs. The first neighbor distance shows a consistent trend of decreasing values with increasing ion momentum. This is an indication of a partial structural transformation within the analysis volume. In the Ar^+ irradiated ribbon we found that the structural modifications were stronger than in the nitrided ribbon, indicating that the driving force of the effect has its origin in structural rather than chemical modification that occur during nitridation. This finding indicates local formation of crystalline phase, like orthorhombic Fe_3B that has first neighbor distance shorter by 6.5% than its amorphous counterpart [17,18]. Nevertheless, such modifications are local, since no indication of long-range order exists in the XRD patterns.

Finally, the corrosion behavior of the ribbons was also studied. Fig. 5 presents the anodic polarization curves of the alloy

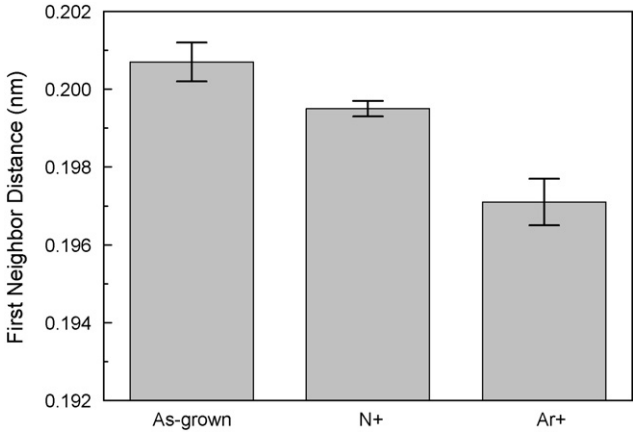

Fig. 4. The first neighbor distance for the three specimens determined by the XRD patterns.

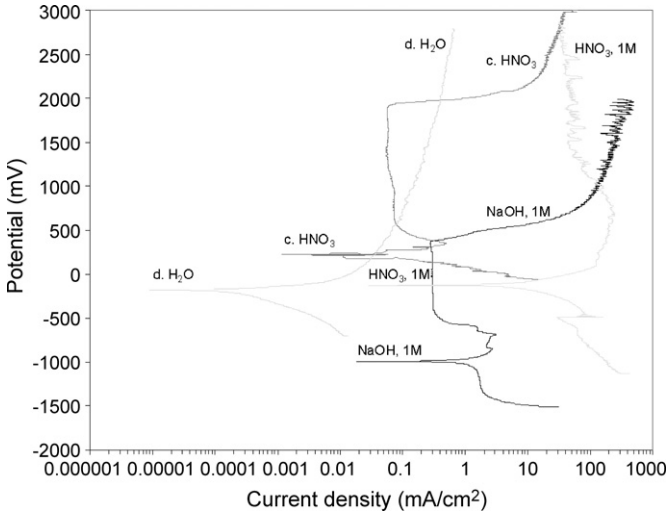

Fig. 5. Potentiodynamic polarization scans of $Fe_{40}Ni_{40}B_{20}$ in d. H_2O, 1M HNO_3, c. HNO_3 and 1M NaOH.

immersed in the d. H_2O, 1M HNO_3, c. HNO_3 and 1M NaOH solutions. The corrosion values extracted (as well as those extracted from chloride solutions) are listed in Table 1. Fig. 5 shows that from a thermodynamic standpoint, the alloy was nobler (higher rest potential) in the c. HNO_3 environment. Deionized water induced the slowest corrosion kinetics (smaller current densities), followed by c. HNO_3. With respect to general corrosion, the alloy corroded fast in 1M NaOH, up to the critical passivation potential, and much faster in HNO_3, 1 M. After the completion of the runs, specimens in c. HNO_3 and 1M NaOH maintained their metallic lustre. The 1M NaOH and c. HNO_3 solutions led to passivation or pseudopassivation, as the anodic curve regions of stable current show, the passivation potential range for the c. HNO_3 being the greatest. Passivation current densities were lower in the c. HNO_3 than in the 1M NaOH electrolyte, indicating higher stability of the protective film in c. HNO_3. This also can be deduced from the significantly higher breakdown potential compared to 1M NaOH. Regarding the nature of the protective film, Mitsuhashi et al. [19] noted that nickel has a positive effect in the corrosion resistance of amorphous alloys due to the formation of a Ni^{2+} oxyhydroxide protective film. Yao et al. [20], detected NiO in the anodically formed passive film of amorphous Mg–Ni alloys and attributed its beneficial effect on the corrosion resistance to its p-type semiconducting properties. Furthermore, it should be mentioned that in crystalline Fe–Ni alloys, the passivity in NaOH solutions may be due to the formation of Fe_3O_4, which has the lowest solubility of all iron oxides in alkaline solutions and also to the outstanding resistance of nickel in NaOH at all concentrations up to the boiling point. The latter is attributed to the formation of NiO [21].

The glassy alloy did not passivate in d. H_2O, but corroded uniformly at a very low corrosion rate, exhibiting excellent corrosion resistance. At potentials higher than the breakdown potential, transpassive dissolution of the specimens immersed in the 1 M NaOH and c. HNO_3 took place resulting in an abrupt increase in the current density. The transpassive dissolution was probably caused by the formation of water soluble compounds. In transition metal alloys, these compounds are formed from higher valence metal cations, such as Fe^{3+} and Ni^{3+}. Regarding nickel crystalline alloys, Hashimoto and Asami have shown that the depassivation process of nickel involves the transformation of nickel hydroxide to hydrated nickelous oxyhydroxide as potential increases [22]. The jagged morphology of the upper part of the anodic curves for the 1M NaOH (esp.) and c. HNO_3 environments, in Fig. 5, may have been caused by the interchangeable formation and dissolution of water soluble compounds.

In the 1M HNO_3 electrolyte, not only was corrosion very fast but also passivation did not occur. Instead, a mainly unstable situation took place as manifested by the jagged morphology of the upper part of the potential–current curve. This state was also caused by the formation and dissolution of water soluble higher valency species, which did not protect from corrosion.

In the chloride environments, the specimens underwent an active to passive transition process at the critical passivation potentials (see Table 1), that resulted in the formation of highly instable surface layers which, in turn, pitted at very active anodic potentials. Regarding general corrosion, active dissolution in the NaCl electrolyte started at a nobler corrosion potential, than in the 1M HCl electrolyte. Also, the corrosion rate in NaCl was significantly lower than the corrosion rate in HCl. The amorphous alloy exhibited slightly less susceptibility to localized corrosion in NaCl, as the slightly higher breakdown potential in NaCl indicates. However, at higher anodic potentials (560 mV for the 3.5% NaCl and 369 mV for the 1N HCl solutions) current density started to decrease, as in a transient stage, to stabilize at a lower current density, indicating a possible repassivation process. The latter was confirmed by cyclic polarization.

Table 1
Corrosion values of amorphous alloy $Fe_{40}Ni_{40}B_{20}$ in various aerated electrolytes, at room temperature

Electrolyte	E_r (mV)	E_{cp} (mV)	E_b (mV)	E_p (mV)	$\Delta E_p = E_b - E_p$ (mV)	E_{pit} (mV)	i_{cor} (mA/cm^2)	r_{cor} (mm/y)
d. H_2O	−190	ad	–	–	–	–	1.8E−3	0.016
1 M HNO_3	−124	134 (ps)	–	–	–	–	14.8	130
c. HNO_3	230	350	1885	599	1286	–	0.035	0.31
1 M NaOH	−990	−680	395	−369	719	–	1.7	14.9
3.5 wt.% NaCl	−311	−244	−149	−209	60	−149	0.008	0.07
1 M HCl	−432	−300	−202	−250	40	−46	0.13	1.14

E_r: rest potential; E_{cp}: critical passivation potential (onset of active to passive transition); E_b: breakdown potential; E_{pit}: localized corrosion potential; ΔE_p: passive range of potentials; E_p: the lowest passivation potential; ad: continuous active dissolution; ps: established pseudopassivity.

4. Conclusions

We studied the surface properties of $Fe_{40}Ni_{40}B_{20}$ glass ribbons before and after irradiation with 200 eV Ar^+ or N^+ ions. The surface of the unprocessed ribbons were found to be rich in Fe at the expense of both Ni and B. After plasma nitridation the relative content of Ni further reduced, while the N incorporation on the surface was equivalent to the sum of concentrations of Fe, Ni and B. XRD experiments have shown that the nearest neighbors in this glass system are the metal–B pairs. After irradiation the nearest neighbor distances were reduced, an effect that we attributed to possible local structural transformations.

The corrosion resistance of $Fe_{40}Ni_{40}B_{20}$ ribbons was excellent in d. H_2O, high in c. HNO_3, very low in 1M NaOH and extremely low in 1M HNO_3. With respect to the chloride environments, the alloy showed high resistance in 3.5 wt.% NaCl but relatively low resistance in 1M HCl. The ribbons can be anodically protected in the c. HNO_3 and 1M NaOH environments, in the passive region of anodic potentials. Protective surface layers were formed at large passivation potential ranges, especially for the c. HNO_3 electrolyte. The ribbons appeared susceptible to localized corrosion in chloride environments. However, there was an indication of repassivation capability.

Acknowledgements

This work has been partially supported by the Greek General Secretariat of Research and Technology and the European Commission, Grant: Pythagoras-II. One of the authors (PP) would like to acknowledge Prof. S. Logothetidis of Aristotle University of Thessaloniki for providing access to the X-ray diffraction equipment.

References

[1] A. Inoue, B.L. Shen, A.R. Yavari, A.L. Greer, J. Mater. Res. 18 (2003) 1487.
[2] A.R. Yavari, W.J. Botta Filho, C.A.D. Rodrigues, A.L. Greer, J.L. Uriarte, G. Huenen, G. Vaughan, A. Inoue, J. Non-Cryst. Solids 304 (2002) 44.
[3] H. Narayan, S.B. Samanta, H.M. Agrawal, R.P.S. Kushwaha, A. Gupta, S.K. Sharma, A.V. Narlikar, D. Kanjilal, Nucl. Instrum. Meth. B 196 (2002) 89.
[4] K.V. Amrute, B.J. Nagare, R.P. Fernandes, V.V. Sivakumar, A. Gupta, D. Kanjilal, D.C. Kothari, Surf. Coat. Technol. 196 (2005) 135.
[5] K. Asami, C.-L. Qin, T. Zhang, A. Inoue, Mater. Sci. Eng. A 375–377 (2004) 235.
[6] A. Gebert, R.V. Subba Rao, U. Wolff, S. Baunack, J. Eckert, L. Schultz, Mater. Sci. Eng. A 375–377 (2004) 280.
[7] H.B. Yao, Y. Li, A.T.S. Wee, Electrochim. Acta 48 (2003) 2641.
[8] A. Dhawan, S. Roychowdhury, P.K. De, S.K. Sharma, J. Non-Cryst. Solids 351 (2005) 951.
[9] M. Mitov, R. Todorova, S. Manev, A. Popov, J. Mater. Sci. Lett. 16 (1997) 1712.
[10] M.G. Alvarez, S.M. Vazquez, F. Audebert, H. Sirkin, Scripta Mater. 39 (1998) 661.
[11] ASTM Standard, G 5-94 (reapproved 1999).
[12] ASTM Standard, G 61-86 (reapproved 1999).
[13] Y. Kucherenko, B. Sinkovic, E. Shekel, P. Rennert, S. Hulbert, Phys. Rev. B 62 (2000) 5733.
[14] L.E. Davis, N.C. McDonald, P.W. Palmberg, G.F. Riach, R.E. Weber, Handbook of Auger Electron Spectroscopy, 2nd ed., Physical Electronics, 1978.
[15] (a) M.J.S. Spencer, A. Hung, I.K. Snook, I. Yarovsky, Surf. Sci. 513 (2002) 389;
(b) C.T. Campbell, Surf. Sci. Rep. 27 (1997) 1.
[16] J.F. Ziegler, J.P. Biersack, U. Littmark, The Stopping and Range of Ions in Solids, Pergamon, New York, 1985.
[17] J. Sietsma, B.J. Thijesse, J. Phys. F 17 (1987) 1.
[18] W.Y. Ching, Y.-N. Xu, B.N. Harmon, J. Ye, T.C. Leung, Phys. Rev. B 42 (1990) 4460.
[19] A. Mitsuhashi, K. Asami, A. Kawashima, K. Hashimoto, Corr. Sci. 27 (1987) 957.
[20] H.B. Yao, Y. Li, A.T.S. Wee, J.W. Chai, J.S. Pan, Electrochim. Acta 46 (2001) 2649.
[21] C.V. D' Alkaine, M.A. Santanna, J. Electroanal. Chem. 457 (1998) 13.
[22] K. Hashimoto, K. Asami, Corr. Sci. 19 (1979) 427.